International Journal of Heat and Mass Transfer 126 (2018) 935–945

Contents lists available at ScienceDirect

International Journal of Heat and Mass Transfer

journal homepage: www.elsevier.com/locate/ijhmt

Temperature field sensing of a thin-wall component during machining: Numerical and experimental investigations

Ammar H. Elsheikh [a,b], Jiajie Guo [a,*], Yang Huang [a], Jingjing Ji [a], Kok-Meng Lee [a,c,*]

[a] The State Key Lab. of Dig. Manuf. and Equip. Tech., Sch. of Mech. Sci. and Eng., Huazhong Univ. of Sci. and Tech., Wuhan 430074, China
[b] Dept. of Prod. Eng. and Mech. Design, Tanta University, Tanta 31527, Egypt
[c] Woodruff Sch. of Mech. Eng. at Georgia Inst. of Tech., Atlanta, GA 30332, USA

ARTICLE INFO

Article history:
Received 16 January 2018
Received in revised form 25 April 2018
Accepted 2 June 2018
Available online 20 June 2018

Keywords:
Heat conduction
Thin-wall plate
Temperature field reconstruction
Modal expansion
Machining

ABSTRACT

Thermal dynamics of hard-to-machined components during manufacturing contributes to micro defects and residual stresses in final products and overheating on machine tools, where temperature plays a critical role in the study of the tool-workpiece interface. However, typical temperature sensing approaches are limited in manufacturing due to their dependence on controlled environments without blockages and cutting fluids/chips, complicated algorithms with long computation time, and knowledge of heat source intensity that is hard to estimate. This paper proposes a temperature field reconstruction (TFR) method as a real-time and online approach to investigate the thermal dynamics of a thin-wall disk-like workpiece (WP) during a turning process. Formulating in a modal expansion with physical laws, the method decouples the temperature field into products of spatially-distributed temperature mode shapes and time-varying modal coefficients that are determined from a finite number of nodal measurements. The TFR method is demonstrated and verified with simulated measurements in finite element analysis, and an illustrative application to TFR during machining is presented to justify its ability for real-time computing and online sensing in manufacturing.

1. Introduction

Thin-wall components, made from hard-to-machined materials and featured with high strength-to-weight ratio, have been in great demands from aviation industries. However, their thermal dynamics during manufacturing contributes to micro defects [1] and residual stresses [2] in final products as well as overheating on cutting tools [3], which deteriorates the final product qualities and shortens the tool-service life. While the temperature plays a critical role in the study of the tool-workpiece interface, it is challenging to monitor the time-varying and spatially-distributed temperature fields under machining conditions [4]. Motivated by the interests to investigate the thermal effects on workpiece (WP) deformations and residual stresses, this paper proposes a temperature field reconstruction (TFR) method as a real-time and online approach to capture the thermal dynamics of a thin-wall disk-like WP during a turning process.

Existing measuring technologies are limited to harsh requirements and hard to implement for process state monitoring in practice. While thermocouples are one of the most widely used methods for measuring temperatures in machining [5,6], they could not be installed on WP surfaces because of the material removal in cutting. Also, it is not practical to embed thermocouples in a WP in a destructive way, although it can be done for one-time trial testing in laboratory studies [7]. As thermocouples provide nodal measurements of temperature, sensor arrays are embedded in machine tools to estimate temperature distributions close to the cutting region [8]. Besides, non-contact approaches such as infrared sensing have been developed for measuring temperature fields. Infrared thermal imaging was used to measure the tool and WP temperatures even at high temperature regions as there is no direct contact with the heat source [9,10]. Though complicated the manufacturing environments are with cutting fluids and chips, thermal images do provide a direct way to capture the temperature distribution across the WP. Considering the small cutting region is usually blocked or obscure in an image, it is desired to develop a method to predict the temperature at the inaccessible region based on information of other measurable locations. Field reconstruction methods have been developed analytically or

---

* Corresponding authors at: The State Key Lab. of Dig. Manuf. and Equip. Tech., Sch. of Mech. Sci. and Eng., Huazhong Univ. of Sci. and Tech., Wuhan 430074, China (J. Guo); Woodruff Sch. of Mech. Eng. at Georgia Inst. of Tech., Atlanta, GA 30332, USA (K.-M. Lee).

E-mail address: jiajie.guo@hust.edu.cn (J. Guo).

https://doi.org/10.1016/j.ijheatmasstransfer.2018.06.006
0017-9310/© 2018 Elsevier Ltd. All rights reserved.

numerically when the physical problems can be mathematically modeled in advance [11–13].

Formulating the thermal dynamics as a boundary value problem (BVP), numerical methods can be employed to reconstruct the distributed temperature fields, among which finite element analysis (FEA) has been widely used [14–18]. With prescribed heating inputs and boundary conditions, the BVP can be solved numerically for the resulting temperature distribution within a targeted space [13,19–22]. This forward approach is well-defined in theory and offers a powerful tool for analysis; however, in manufacturing practices, heat sources are usually unknown and immeasurable because they are affected by cutting processes. Similarly, the assumptions of ideal boundary conditions, such as the Dirichlet's condition [21–26], could lead to modeling errors and thus affect the sensing accuracy in practical applications. To estimate the unknown heat source, inverse approaches have been developed for applications of metal casting [27], welding [28], forming [29] and machining [30–32], and different methods have been proposed such as the least square inverse scheme [33,34], golden section technique [35,36], conjugate gradient method [37,38], local meshless method [39,40], sequential function specification method [41,42]. Most inverse approaches involving iterations are usually too time consuming for real-time applications. In another way, heat generated in metal cutting can be estimated using measured cutting forces and other cutting parameters, such as depth of cut, feed-rate and cutting speed [43]. Recently, the flexible division algorithm is developed with the time-efficiency of 100 ms for real-time prediction of the temperature in cutting with the heat flux estimated from an energy equation and cutting force measurements [13].

As dynamics of physical fields conforms to certain governing partial differential equations whose solutions are derived with the separation of variables, general solutions can be obtained as a summation of eigenfunctions or mode shapes. In this way, displacement and strain fields are reconstructed across a thin-wall WP under machining based on prior knowledge of vibration mode shapes and finite number of nodal measurements [12]. This paper proposes a TFR method as a real-time and online approach to investigate the thermal dynamics of a thin-wall disk-like WP during a turning process. This method does not require expensive instruments, complicated algorithms or even knowledge of heating source intensity in prior, so it provides a simple yet effective approach for process state monitoring in manufacturing. The remainder of this paper offers the following:

- By formulating the WP thermal dynamics as a boundary value problem, the proposed TFR method is developed with modal expansion techniques, where the spatially distributed information and time-varying factors are decoupled, so that the temperature field can be determined from a finite number of nodal measurements.
- Demonstrating the proposed TFR method via modal analysis, dimensionless variable groups are introduced to study effects of material properties on field reconstruction, based on which a guideline is provided to determine the modes employed in reconstruction.
- The TFR method is numerically verified with simulated measurements using FEA, and an illustrative application to TFR during machining is presented to justify its ability for real-time computing and online sensing in manufacturing.

2. Problem formulation

As shown in Fig. 1, the thermal dynamics of a rotating WP under lathe-machining is modeled as a thin circular plate (of radius a and thickness h) subjected to the heat source at the tip of the cutting tool. A polar coordinate is established at the plate center where the r and θ axes span the plate mid-surface and the z-axis is collinear with the WP rotation axis. Because the heat conduction rate is much slower than the rotation speed Ω, the thermal dynamics is dominated by the rotational effect and is assumed to be axisymmetric. The heat source at the cutting position ($r = r_c$, $z = z_c$) is described by the energy generation (W/m^3) of $g(t, r, z) = g_1(t)\delta(r - r_c)\delta(z - z_c)$ characterizing any heat generated during cutting or dissipated into environments. The top ($z = h/2$) and bottom ($z = -h/2$) plate surfaces are subjected to convection while the radial boundary ($r = a$) is thermally insulated given the large aspect ratio (a/h). The initial temperature is set to the room temperature. It is desired to obtain the dynamic temperature distribution across the WP, especially the temperature at the cutting region which is inaccessible in practice.

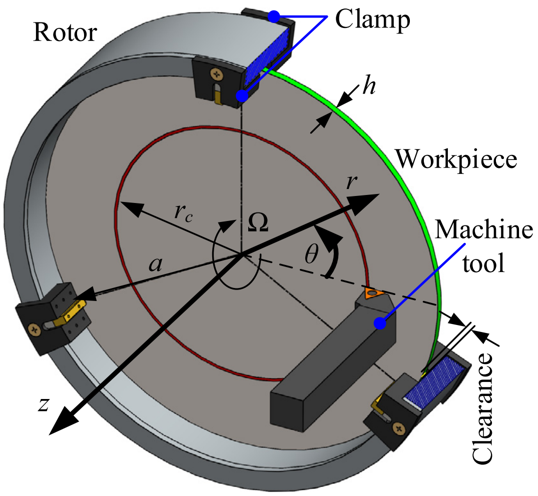

Fig. 1. A circular plate with an axisymmetric heat source.

The temperature distribution $T(t, r, z)$ across the plate is governed by the following partial differential equation

$$\frac{\partial^2 T}{\partial r^2} + \frac{1}{r}\frac{\partial T}{\partial r} + \frac{\partial^2 T}{\partial z^2} + \frac{1}{k_t} g(t, r, z) = \frac{1}{\alpha}\frac{\partial T}{\partial t}, \quad 0 \leqslant r \leqslant a, \; -\frac{h}{2} \leqslant z \leqslant \frac{h}{2} \tag{1}$$

where k_t is the thermal conductivity, and the thermal diffusivity (m^2/s) is defined as $\alpha = k_t/(\rho C_p)$ with ρ and C_p denoting the density and specific heat, respectively.

Initially, the temperature distribution on the WP is uniformly equal to the initial temperature T_0

$$T|_{t=0} = T_0 \tag{1$'$a}$$

and the boundary condition on the plate surface is provided by

$$T|_{r=0} < \infty, \; \partial T/\partial r|_{r=a} = 0 \tag{1$'$b, c}$$

$$(k_t \partial T/\partial z + k_c T)|_{z=h/2} = k_c T_\infty, (k_t \partial T/\partial z - k_c T)|_{z=-h/2} = -k_c T_\infty \tag{1$'$d, e}$$

where T_∞ is the ambient temperature; the convection heat-transfer coefficient is calculated via $k_c = 0.335 k_a \sqrt{\Omega/\nu}$ [44]; and k_a, ν and Ω are the heat conductivity, air kinematic viscosity and angular velocity, respectively. It is noted that k_a and ν are temperature-dependent; and for a disk temperature ranging between 20 °C and 220 °C, k_c is approximated as 20 W/m^2 K with Ω = 800 rpm to emulate the axisymmetric case under high-speed turning. In practice, the initial and ambient temperatures, T_0 and T_∞, are usually the same.

To estimate the temperature at the tool-WP interface, it is desired to develop a novel reliable and efficient method to reconstruct the temperature field across the WP under machining conditions. Typical forward approaches to calculate the temperature field governed by (1) requires knowing all inputs and boundary conditions as well as parametric values. While the material thermo-physical properties can be obtained in advance, the heat source intensity is hard to estimate during machining and only nodal temperatures far from the tool-WP interface are practically measurable. In this way, the proposed field reconstruction method only employs the measured temperature at a finite number of sensing locations, which does not require the knowledge of the heating input. Specifically, the temperature field is reconstructed with mode shapes obtained from dynamic analysis of (1).

3. Temperature field reconstruction

The thermal dynamic analysis is carried out for TFR, where the time-varying temperature distribution is expanded with mode series and the modal coefficients will be determined by experimental measurements. To facilitate the analysis, the above problem is reformulated by homogenization of the boundary conditions (1′d, e) and separation of the variables. Then, the closed-form solution, obtained via the Green's function approach, is used to justify the number of employed mode shapes.

3.1. Transient response

The temperature field $T(t, r, \theta)$ can be divided into two components, $T = T_\infty + \psi$, the constant ambient component T_∞ satisfying (1) with $g(t, r, z) = 0$ and the dynamic component ψ satisfying the following:

$$\frac{\partial^2\psi}{\partial r^2}+\frac{1}{r}\frac{\partial\psi}{\partial r}+\frac{\partial^2\psi}{\partial z^2}+\frac{1}{k_t}g=\frac{1}{\alpha}\frac{\partial\psi}{\partial t},\quad 0\leqslant r\leqslant a,\ -\frac{h}{2}\leqslant z\leqslant\frac{h}{2} \tag{2}$$

$$\psi|_{t=0}=T_0-T_\infty \tag{2$'$a}$$

$$\psi|_{r=0}<\infty,\ \partial\psi/\partial r|_{r=a}=0 \tag{2$'$b, c}$$

$$(-k_t\partial\psi/\partial z-k_c\psi)|_{z=h/2}=0,\ (k_t\partial\psi/\partial z-k_c\psi)|_{z=-h/2}=0 \tag{2$'$d, e}$$

Employing the separation of variables $\psi(t,r,z)=\psi_1(t)\,\psi_2(r)\,\psi_3(z)$, the homogeneous BVP (2) and (2′) (temporarily setting $g = 0$ for modal analysis) is decoupled into the following:

Governing equations	Initial/boundary conditions	
$\dot{\psi}_1+\alpha\lambda^2\psi_1=0$	$\psi_1(0)=1$	(3a)
$r\ddot{\psi}_2+\dot{\psi}_2+\delta^2 r\psi_2=0$	$\psi_2(0)<\infty,\dot{\psi}_2(a)=0$	(3b)
$\ddot{\psi}_3+\beta^2\psi_3=0$	$(-k_t\dot{\psi}_3-k_c\psi_3)\big\vert_{z=h/2}=0,(k_t\dot{\psi}_3-k_c\psi_3)\big\vert_{z=-h/2}=0$	(3c)

The solutions to the above initial/boundary value problems are obtained as

$$\psi_1(t)=e^{-\alpha\lambda_{ij}^2t} \tag{4a}$$

$$\psi_2(r)=J_0(\delta_i r)\quad\text{with}\quad J_0'(\delta_i a)=0 \tag{4b, c}$$

$$\psi_3(z)=\cos\left[\beta_j z-\frac{1-(-1)^j}{4}\pi\right]\quad\text{with}\quad\tan h\beta_j=\frac{k_t k_c\beta_j}{k_t^2\beta_j^2-k_c^2} \tag{4d, e}$$

where J_0 is the first kind of Bessel functions with the zeroth order, δ_i's and β_j's are eigenvalues determined from the boundary conditions (4c,e) and λ_{ij}'s are given by $\lambda_{ij}^2=\delta_i^2+\beta_j^2$ $(i, j = 0, 1, 2, \ldots)$.

Then, the solution to the BVP (2) and (2′) can be obtained as

$$\psi(t,r,z)=\sum_{i=0}^{\infty}\sum_{j=0}^{\infty}q_{ij}(t)\Phi_{ij}(r,z) \tag{5}$$

where Φ_{ij}'s are the temperature mode shapes obtained from (4) to characterize the spatial distribution, and the time-varying modal coefficients q_{ij}'s are derived in Appendix A:

$$\Phi_{ij}(r,z)=J_0(\delta_i r)\cos\left[\beta_j z-\frac{1-(-1)^j}{4}\pi\right] \tag{5$'$a}$$

$$q_{i0}(t)=\frac{\beta_0}{\beta_0 h+S_{\beta_0 h}}\frac{4r_c\Phi_{ij}(r_c,z_c)}{k_t a^2J_0^2(\delta_i a)}\frac{1-e^{-\alpha\lambda_{ij}^2t}}{\lambda_{ij}^2},$$
$$q_{ij}(t)=\frac{4r_c\Phi_{ij}(r_c,z_c)}{k_t h a^2J_0^2(\delta_i a)}\frac{1-e^{-\alpha\lambda_{ij}^2t}}{\lambda_{ij}^2}\quad(j=1,2,\ldots) \tag{5$'$b}$$

As the difference between T and ψ is only the constant T_∞, the temperature field is represented by $\psi(=T - T_\infty)$ in the following analysis.

3.2. Field reconstruction procedure

Once the modal coefficients q_{ij}'s are calculated, the temperature field ψ can be reconstructed with superposition of mode shapes Φ_{ij} as indicated in (5). The detailed reconstruction procedure is formulated in the following. The serial summation in (5) can be rearranged as

$$\psi(t,r,z)=\sum_{k=1}^{\infty}q_k(t)\Phi_k(r,z) \tag{6}$$

and the estimated quantity can be approximated by the modes of the lowest K orders:

$$\tilde{\psi}(t;r,z)=\sum_{k=1}^{K}q_k(t)\Phi_k(r,z) \tag{6$'$}$$

With measured ψ at N different locations (r_n, z_n), $n = 1, 2, \ldots, N$, q_k's can be obtained from (7):

$$\mathbf{q}=\left(\mathbf{S}^{\mathrm{T}}\mathbf{S}\right)^{-1}\mathbf{S}^{\mathrm{T}}\tilde{\Psi} \tag{7}$$

where

$$\tilde{\Psi}=\left[\tilde{\psi}(t,r_1,z_1)\ \tilde{\psi}(t,r_2,z_2)\ \cdots\ \tilde{\psi}(t,r_n,z_n)\right]^{\mathrm{T}},\ \mathbf{q}(t)=[q_1\ q_2\ \cdots\ q_K]^{\mathrm{T}},$$

$$\text{and} \quad \mathbf{S} = \begin{bmatrix} \Phi_1(r_1,z_1) & \Phi_2(r_1,z_1) & \cdots & \Phi_K(r_1,z_1) \\ \Phi_1(r_2,z_2) & \Phi_2(r_2,z_2) & \cdots & \Phi_K(r_2,z_2) \\ \vdots & \vdots & \ddots & \vdots \\ \Phi_1(r_N,z_N) & \Phi_2(r_N,z_N) & \cdots & \Phi_K(r_N,z_N) \end{bmatrix}.$$

Using N sensing points and K modes for the reconstruction process, there are N knowns (organized in the $N \times 1$ vector $\tilde{\Psi}$) and K unknowns (the $K \times 1$ vector $\mathbf{q}$), where $N \geq K$ is enforced for a determined or over-determined problem to guarantee a unique solution. While the mode shapes Φ_{ij}'s are obtained offline and stored in a database, the coefficient vector $\mathbf{q}$ is real-time calculated with online measurements, then the temperature field ψ across the plate is approximated and calculated using $(6')$. It is noted that the reconstructed $\tilde{\psi}$ is a smooth field; local discontinuities caused by inputs, such as steps or impulses, can be retrieved with interpolation or extrapolation from reconstructed data close to the discontinuous regions.

3.3. Asymptotic and normalized analyses

The non-dimensional groups in (8a-e) are defined to account for the material properties effects on the temperature field and facilitate the parametric analysis for a guideline of selecting mode shapes in the field reconstruction:

$$\frac{R}{r/a} = \frac{Z}{z/h} = \frac{\bar{\delta}}{\delta a} = \frac{\bar{\beta}}{\beta h} = \frac{\bar{q}_{ij}}{q_{ij}/\gamma_{ij}} = 1 \tag{8a-e}$$

$$\text{where} \quad \gamma_{ij} = a \bigg/ \left(\lambda_{ij}^2 \int_0^a \int_{-h/2}^{h/2} r' \Phi_{ij}^2(r', z') dr' dz' \right) \tag{8f}$$

Determination of β's in (4e) is equivalent to the following two equations:

$\tan \beta_j h/2 = k_c/(k_t \beta_j)$ and $\cot \beta_j h/2 = -k_c/(k_t \beta_j)$.

For a small β_j, the approximation $\beta_j h/2 \simeq k_c/(k_t \beta_j)$ gives rise to

$$\beta_0 \simeq \sqrt{2k_c/(hk_t)}; \tag{9a}$$

as $\beta_j \to \infty$, the zeros of $\tan \beta_j h/2$ and $\cot \beta_j h/2$ can be used as the asymptotic estimates of β_j's:

$$\beta_j \simeq j\pi/h \quad (j = 1, 2, \ldots) \tag{9b}$$

Then the normalized β_j's are $\bar{\beta}_0 \simeq \sqrt{2hk_c/k_t}$ and $\bar{\beta}_j \simeq j\pi$, and the q_{ij}'s (derived in Appendix A) are normalized as $\bar{q}_{ij}(t) = (1 - e^{-\alpha\lambda_{ij}^2 t}) R_c \Phi_{ij}(R_c, Z_c)/k_t$ (i and j = 0, 1, 2 ...) for a unit input. It is noted that the intensity and location of an applied heat source are accounted by $\bar{q}_{ij}$ while γ_{ij} characterizes the weighted effects of each mode on the final output.

4. Numerical verification and illustrative example

The simulated results are presented for different materials to justify approximations in the above formulation and verify the proposed field reconstruction method with FEA, where the material properties are listed in Table 1. Four groups of results are organized for the following objectives:

(1) *Normalized eigenvalue analysis* is carried out to investigate effects of material properties and plate dimensions on the distributions of eigenvalues.
(2) *Mode shapes* are simulated to illustrate the temperature distributions in each mode.
(3) *Weighted modal coefficients* are investigated and compared to provide a guideline to determine the dominant modes.
(4) *Illustrative examples* are presented to verify the TFR method using simulated measurements in FEA.

4.1. Normalized eigenvalue analysis

The eigenvalues δ_i's and β_j's are numerically calculated as the zeros of (4c) and (4e) respectively, and λ_{ij}'s are evaluated using $\lambda_{ij}^2 = \delta_i^2 + \beta_j^2$ (i, j = 0, 1, 2, ...) in the following way:

$$\frac{(1/\lambda a)^2}{(1/\bar{\delta})^2} + \frac{(1/\lambda h)^2}{(1/\bar{\beta})^2} = 1 \tag{10}$$

Then the normalized analysis of eigenvalues is presented in the following:

- Fig. 2(a) plots the Bessel function J_0 and its derivative against the normalized variable $\bar{\delta}$. The eigenvalues are obtained from the depicted roots of J_0', where the smallest $\bar{\delta}$ is zero and they increase with the order (subscript i) in an asymptotical period of π. It is noted that only the lowest orders will be employed in the reconstruction, so the first few eigenvalues are numerically calculated. Besides, δ_i's are only related to the outer radius a and independent of material properties.
- As shown in the logarithmic plots (Fig. 2b and c), β_j's are obtained at the local minimum peaks of $|f(\beta)|$ which are equivalent to the zeros of (4e). Fig. 2(b) shows that β_0 of different materials increases with the decreasing thermal conductivity k_t for the same thickness h. As β_j's increase in Fig. 2(c), different curves of $|f(\beta)|$ for various materials collapse into one and β_j's are found as integer times of π/h. On the other hand, when normalizing β_0 with respect to the material properties as shown in Fig. 2(d), a straight line is obtained in the logarithmic scale between β_0 and h. So Fig. 2(c) and (d) verify the asymptotic results of (4d, e), where the material properties only affects β_0 while β_j's (j = 1, 2, ...) are proportional to $1/h$.
- Fig. 2(e) shows ellipses defined by (10) with coordinates ($1/\lambda_{ij}a$, $1/\lambda_{ij}h$) in the first quadrant for positive λ_{ij}'s, where the lengths of principal axes are $1/\bar{\delta}_i$ and $1/\bar{\beta}_j$. So each of the ellipses can be denoted by their geometric features $(\bar{\delta}_i, \bar{\beta}_j)$. Given any slenderness of a circular plate, a straight line can be drawn by passing through the origin at a slope of a/h. Then the coordinate of the intersecting point between the straight line and an ellipse $(\bar{\delta}_i, \bar{\beta}_j)$ will lead to the eigenvalue λ_{ij}. This is the geometric interpretation of the relation among δ, β and λ and

Table 1
Material properties.

Materials	Density ρ (kg/m^3)	Conductivity k_t (W/m-K)	Specific heat C_p (J/kg-K)	Diffusivity α (10^{-6} m^2/s)
Copper	8960	401	385	116.25
Aluminum	2700	200	900	82.31
AISI 4340	7850	44.5	475	11.93
Inconel 718	8190	11.4	435	3.20
Ti-6Al-4V	4430	6.7	526	2.88

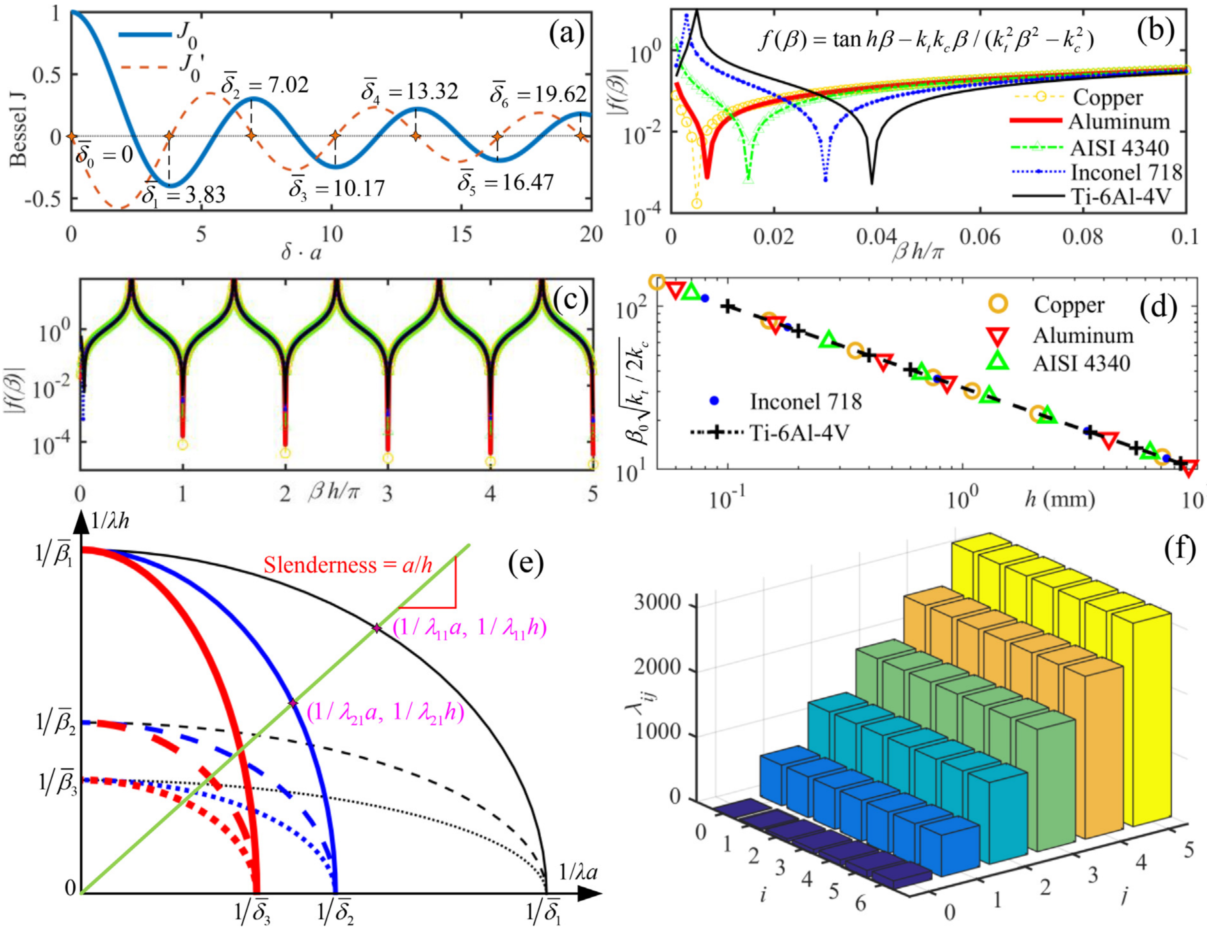

Fig. 2. Illustration of eigenvalues: (a) Distribution of δ_i; (b) normalized β_0 for different materials; (c) normalized β_j for different materials; (d) effect of h on β_0; (e) the relation among eigenvalues and geometries; (f) λ_{ij} for aluminum.

it is valid for different materials. It is noted that $\lambda_{0j} = \beta_j$ and $\lambda_{i0} = \sqrt{\delta_i^2 + 2k_c/hk_t}$ are not included for analysis. It can be visualized from Fig. 2(e) that the intersecting points approach towards the origin with an increasing order of $(\bar{\delta}_i, \bar{\beta}_j)$, indicating that λ_{ij}'s increase with i and j. It is also observed that β_j's play a more significant effect on λ_{ij}'s than δ_i's for a thin-wall plate that is represented by a straight line of a large slope a/h. This observation is verified by taking an aluminum plate (a = 150 mm, h = 5 mm) for example in Fig. 2(f).

4.2. Temperature mode shapes

Given the calculated eigenvalues of δ_i's and β_j's, the temperature mode shapes are simulated using (5$'$a) where the lowest orders are used for illustration. As the mode shapes are obtained by the product of ψ_2 and ψ_3 in (4b,d), Fig. 3 plots the eigenfunctions for different eigenvalues in the normalized coordinates. The Bessel function ψ_2 has a maximum value of unity at the disk center and then fluctuates and decreases along the radius; while the sinusoidal function ψ_3 oscillates at a frequency of $j\pi$ (rad/s), and at the disk mid-plane $\psi_3 = 0$ for an odd j and $\psi_3 = 1$ for an even j. It is noted that for the zeroth order ψ_2 is a constant one because $\delta_0 = 0$, while ψ_3 appears like a constant due to the small plate thickness. It is also observed that the subscripts i and j indicate the number of zeros of the corresponding ψ_2 and ψ_3 whose number of peaks is equal to $i + 1$ and $j + 1$, respectively. The above properties characterize the geometric features of mode shapes as illustrated in Table 2, where the temperature along the dashed lines is zero.

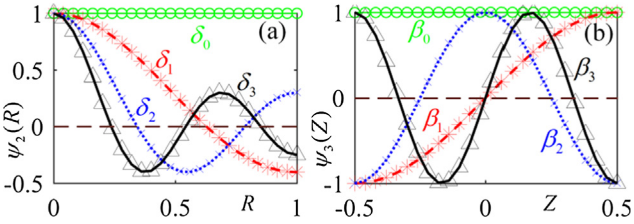

Fig. 3. Illustration of eigenfunctions: (a) ψ_2 against normalized r; (b) ψ_3 against normalized z.

4.3. Weighted modal coefficients

The coefficients γ_{ij}'s from (8f) indicate the contribution of each modes in the temperature field, thus the values of these weighted modal coefficients provide a guideline to select mode shapes for reconstruction in (6$'$). The bar charts in Fig. 4(a) show the γ_{ij}'s values for aluminum and titanium alloy in the range of $0 \le i \le 15$ and $0 \le j \le 14$. It is observed that the weights of orders with $j \ge 1$ are negligible because γ_{ij}'s are reciprocal of λ_{ij}'s that increase drastically with j (Fig. 2f); while the lowest orders with $j = 0$ dominate the temperature field. Besides, the subplot in Fig. 4(a) compares the coefficients for $j = 0$ among different materials (Table 1). It is shown that the lowest order ($i = 0$, $j = 0$) for copper and aluminum provides the largest weight compared to the others, while the

Table 2
Mode shapes.

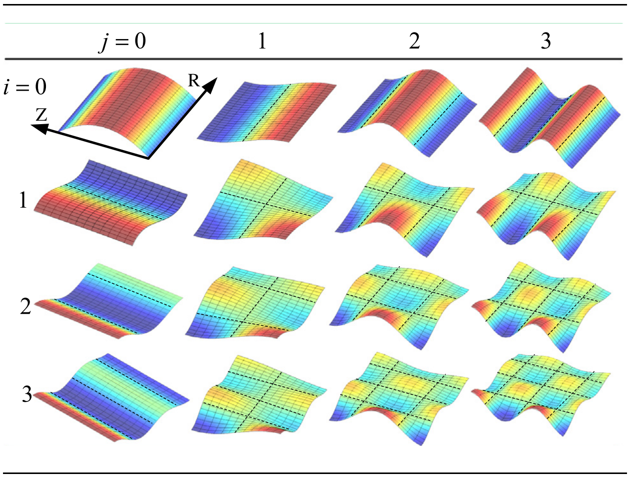

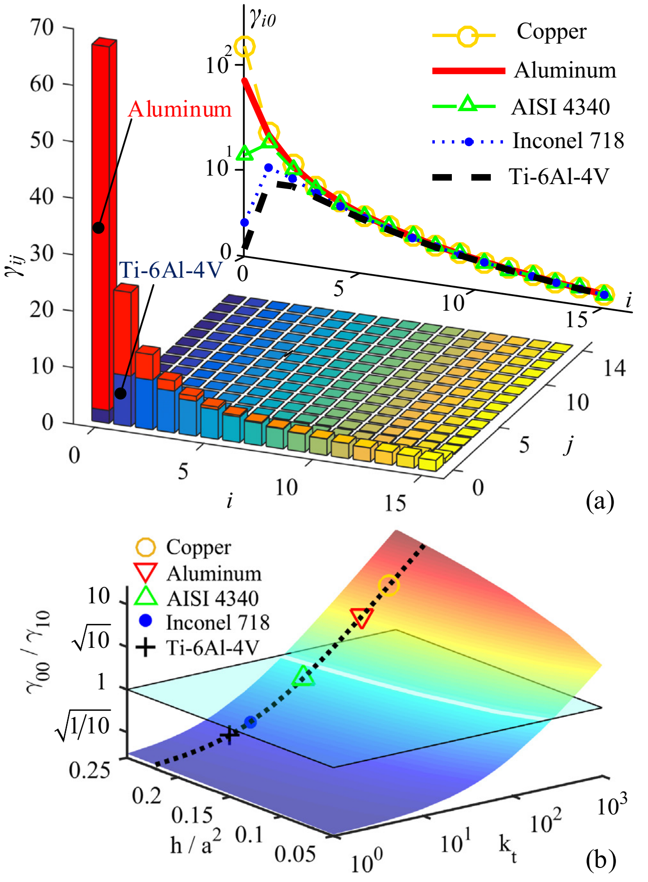

Fig. 4. Distribution of weighted modal coefficients.

largest modal weights for Steel AISI 4340, Inconel 718 and Ti-6Al-4V come from the order ($i = 1, j = 0$). This can be explained by the ratio (Appendix B)

$$\frac{\gamma_{00}}{\gamma_{10}} = \frac{J_0^2(\bar{\delta}_1)}{J_0^2(\bar{\delta}_0)}\left(1+\frac{\bar{\delta}_1^2}{2\pi k_c}Vk_t\right)$$

where V is the plate volume, $J_0^2(\delta_1 a)/J_0^2(\delta_0 a)$ is the same for different materials, thus γ_{00}/γ_{10} can be plotted as a function of V and k_t as shown in Fig. 4(b).

4.4. Illustrative examples

The proposed TFR method is numerically verified with FEA in COMSOL, where an axisymmetric heating source (intensity of $P = 120$ W) is applied on the top surface ($r_c, z_c = h/2$) of a thin circular plate, and the sensing points are allocated on the bottom surface ($r_i, i = 1, 2, \ldots, N, z_c = -h/2$). The ambient temperature T_0 is taken as 20 °C. Two illustrative examples are presented with aluminum for Case 1 and titanium alloy for Case 2, where the parametric values for simulation are listed in Tables 1 and 3. The FEA results for both cases are shown in Fig. 5(a) and (b) that the titanium plate embodies much higher peak temperature at the heating zone and larger variation (difference between maximum and minimum temperatures) than the aluminum plate, even though the input power density $g_1(=P/2\pi r_c)$ for Case 2 is smaller than that of Case 1. This is because the conductivity k_t of titanium is much smaller than that of aluminum. In this way, Fig. 5(c) plots the temperature ratio against k_t for different materials, where T_t and T_b are the steady-state temperatures simulated in FEA at the points (r_c, $h/2$) and (r_c, $-h/2$), respectively, and the regression curve (plotted in a red dashed line) is obtained as

$$T_t/T_b = 1 + 1.1792e^{-1.4543\log_{10}k_t}. \qquad (11)$$

The field reconstruction procedure is demonstrated in the following:

(1) The temperature field outside the heating region is reconstructed using (6) with K modes and N nodal temperatures obtained on the bottom surface.
(2) The temperature T_t at the heating point is estimated using (11) with the reconstructed T_b.
(3) The temperatures within the heating region are interpolated with T_t and the reconstructed data adjacent to the heating region boundary (Table 3).

The reconstructed results are shown in Fig. 6 where the upper and bottom rows are for Case 1 and Case 2, respectively. The reconstructed temperatures on both surfaces ($z = \pm h/2$) are plotted along the radius and compared with FEA in Fig. 6(a) and (b). Temperatures are very close on both surfaces far away from the heating region because of the small thickness, while within the heating region the temperatures rise dramatically as it gets closer to the heating sources. The reconstruction formula ($6'$) is good at capturing smooth distributions that are distant from the impulses in these cases, so the peak temperatures must be estimated from (11) and the temperature fields in the heating region are obtained with interpolation. Revolving the reconstructed curves around the z-axis, the temperatures across the disk upper surfaces are embedded in Fig. 6(a) and (b) to compare with the FEA results in Fig. 5. The temperatures distributed in the cross-section areas are shown in Fig. 6(c) and (d) with the dashed lines indicating the boundaries of the heating regions. The sizes of the heating regions, symmetric with the heating points, are estimated from the slopes of the reconstructed curves ($z = -h/2$) as the temperature gradient increases as it gets closer to the heat source. Fig. 6(e) and (f) plot the errors between the reconstructed fields and FEA results, where the maximum percentage errors are 1.12% and 6.48% for aluminum and titanium, respectively, at the heating point. It is noted that the ripples in errors along the radius are due to neglection of higher order modes in the approximation. In other words, the errors will decrease by employing more mode shapes in reconstruction. It costs about 0.07 and 0.1 s in Cases 1 and 2, respectively, for reconstruction with spatial resolutions of 1 mm in the r direction and 0.1 mm in the z direction on a desktop computer (Intel i7 CPU 3.5 GHz, 32 GB RAM). Fig. 6(g) and (h) plot the percentage errors between the reconstructed temperature fields and the FEA results

Table 3
Design configuration for field reconstruction.

Case	r_c (mm)	K	N	r_i (mm)	Heating region
1	75	5	6	10, 40, 60, 100, 130, 150	$60 \le r \le 90$ mm
2	123	8	9	10, 30, 50, 70, 90, 110, 120, 130, 150	$117 \le r \le 129$ mm

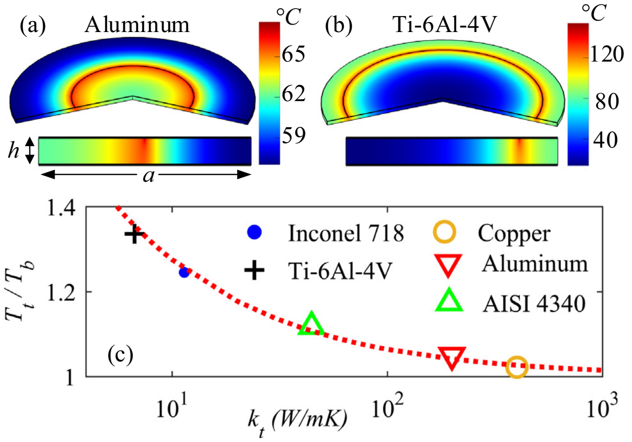

Fig. 5. Finite element analysis: (a) Case 1; (b) Case 2; (c) Ratio of temperatures.

on the upper surface for an increasing K to examine the error convergence in both reconstruction cases. The sensing nodes are equally distributed along the radius with $N = K$. It can be observed that overall, the percentage errors decay when more mode shapes are employed for reconstruction. While the errors in the region near the boundaries and the heating source tend to be large, they decrease with an increasing K. Furthermore, the root-mean-square errors (RMSEs) between the TFR and FEA results can also be calculated, which are

(0.369, 0.101, 0.088 and 0.081 °C) for K (=3, 6, 9 and 12) in Case 1; and
(9.431, 6.677, 1.241, 1.144 and 1.015 °C) for K (=2, 5, 8, 12 and 16) in Case 2.

The RMSEs verify the error convergence with an increasing number of mode shapes.

While the thermal properties of materials are temperature-dependent in practice, their nominal values (Table 1) are used for the TFR here; the approximations are to be verified with an FEA. Given the steep temperature-gradient for Case 2 in Fig. 6, the realistic thermal properties of titanium alloy ($600 < C_p \le 750$ J/kg-K and $6 < k_t < 20$ W/m-K for $0 < T \le 1000$ °C) [45] are employed to simulate the temperature distributions in COMSOL for different heat source intensities $P = 20$ W, 120 W and 240 W. The reconstructed temperature fields, which were obtained with the same setup as in Table 3, match with the FEA results on both surfaces as shown in Fig. 7, where the RMSEs are listed in Table 4. Although the errors increase with P or the maximum temperature $T_{\max}$, the percentage errors (estimated at about 1%) are very small. Thus, the TFR method is robust with errors in material properties, because it is not built on material models but actual measurements. Since the measured data represent the material effects on temperature distributions, the material property approximation is well compensated during reconstruction. Besides, the mode

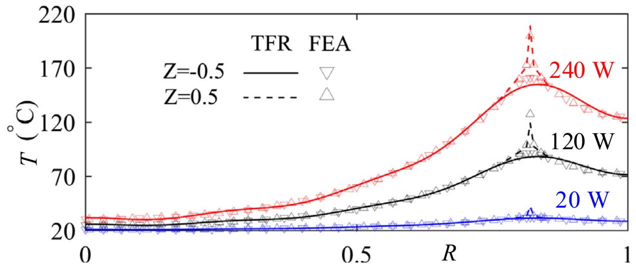

Fig. 7. Verification with temperature-dependent material properties.

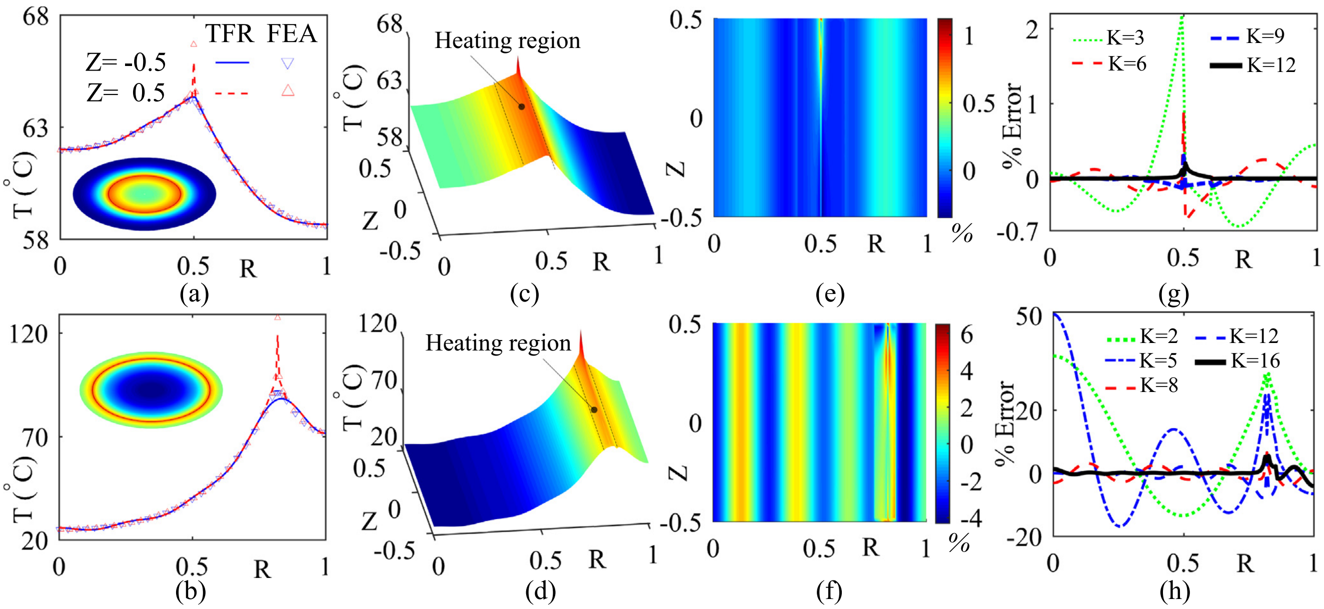

Fig. 6. Reconstructed temperature fields: (a and b) Temperature distributions on both surfaces; (c) and d) Reconstructed temperature fields in cross sections; (e and f) Errors of reconstructed temperatures; (g and h) Convergence analysis of reconstruction errors. The upper row is for Case 1 and the bottom row is for Case 2.

Table 4
RMSE for different heat source intensities.

P (W)	$T_{\max}$	RMSE (Z = −0.5)	RMSE (Z = 0.5)
20	35.87	0.21	0.57
120	127.28	1.19	1.24
240	199.56	2.19	2.05

Unit: Celsius degree.

Table 5
Specifications of Fluke Ti400 infrared camera.

Specifications	Values
Range	−20 °C to +1200 °C
Accuracy	±2 °C or 2% (whichever is greater)
Contrast	≤0.05 °C at 30 °C
Frequency	9 Hz or 60 Hz sampling rate
Detector type	Focal Plane Array (320 × 240 pixels)
Spectral band	7.5–14 μm

shapes as well as the eigenvalues normalized with respect to the dimensions and material properties also help to improve the robustness of the TFR method.

5. Experiment results and illustrative application

The reconstruction of temperature fields has been experimentally evaluated on the a custom-designed duplex lathe-turning center (DLTC) [13]. As shown in Fig. 8, a Ti-6Al-4V disk-like WP (with thermal properties given in Table 1, a = 150 mm, h = 5 mm) was secured on the rotor by three equally spaced clamps at its outer perimeter. In this study, the DLTC was modified with one cutting tool being applied (on one side of the WP) and an IR imager (on the other side of the WP) for clear illustration of experimental validation. The WP was rotated at a speed of 100 r/min and machined with 0.5 mm depth of cut by the tool feeding radially starting from r_c = 119 mm towards the WP center at 0.05 mm/s. To facilitate the IR measurements, a thin thermal-grease layer (thickness <0.5 mm, emissivity $\varepsilon = 0.95$, $k_t \approx 1.5$ W/m-K) was applied on the WP (black surface in Fig. 8), based on which the emissivity calibration was carried out before the cutting tests [46]. Specifications of the infrared thermal imager (Fluke Ti400) are listed Table 5. The reconstruction is performed using the same configuration as Case 2 in Table 3. Two sets of results are provided, where the transient temperature field is investigated in the first set and the steady state is studied in the second one.

The transient response of the WP temperature to the onset of cutting is demonstrated in Fig. 9. As observed in the thermal image in Fig. 9(a), the temperatures of the regions (I, II and III) closest to the clamps along the cutting trajectory are the highest while the regions (IV, V and VI) among the clamps are cooler, where the highest and lowest temperatures are denoted in red and blue respectively. This is because the WP dynamics gives rise to the distributed deformations across the WP, where a smaller WP vibration displacement results in a larger depth of cut thus a higher temperature when it is closer to the clamps, which is indicated from the dominant vibration mode shape in Fig. 9(b). In this way, the reconstructed results along the higher-temperature radii (I, II and III)) are averaged and compared against the experimental data captured on the measured surface ($z = -h/2$); the temperature on the machined surface ($z = h/2$) is also reconstructed. The peak temperatures are estimated as 30.48 °C and 41.27 °C on the measured and machined surfaces, respectively, in Fig. 9(c). The same procedure is carried out for the lower-temperature radii (IV, V and VI), and the peak temperatures are 27.19 °C and 36.83 °C on the measured and machined surfaces, respectively, in Fig. 9(d). Revolving the temperature distributions on the WP cross sections, the temperature fields are obtained on the measured and the machined surfaces as embedded in Fig. 9(c) and (d). The reconstructed field is validated by comparing Fig. 9(c) with the thermal image in Fig. 9(a), and the temperature field in the cutting region is predicted with a much larger gradient (Fig. 9d) than that on the other surface.

As the turning process was stabilized and the temperature distribution arrived at the steady state, the thermal image is shown in Fig. 10(a) that the temperatures are homogeneous in the tangential direction, and the reconstructed results along three radii are averaged and plotted for both surfaces for the WP where the peak temperatures are evaluated as 32.61 °C and 44.00 °C. Then the

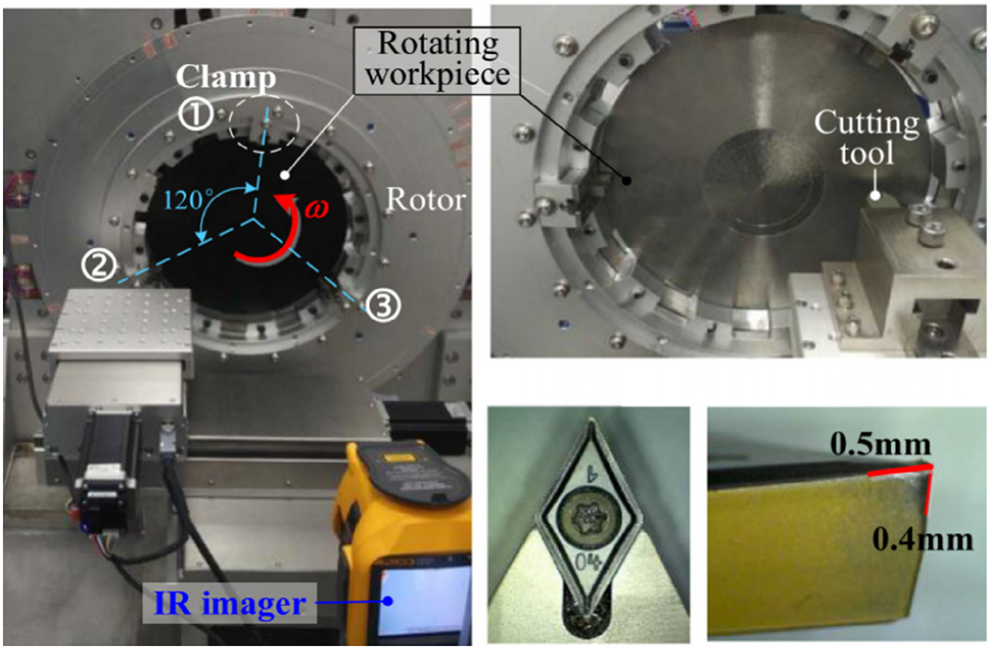

Fig. 8. Experimental setup on the duplex lathe-turning center [13].

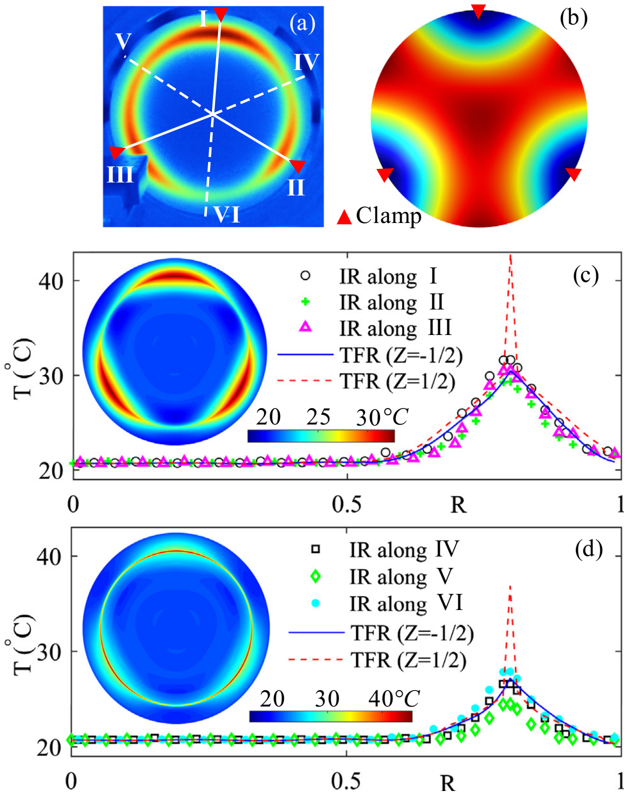

Fig. 9. Reconstruction of transient temperature fields: (a) Thermal image; (b) Dominant vibration mode shape; (c) Reconstruction along I, II and III; (d) Reconstruction along IV, V and VI.

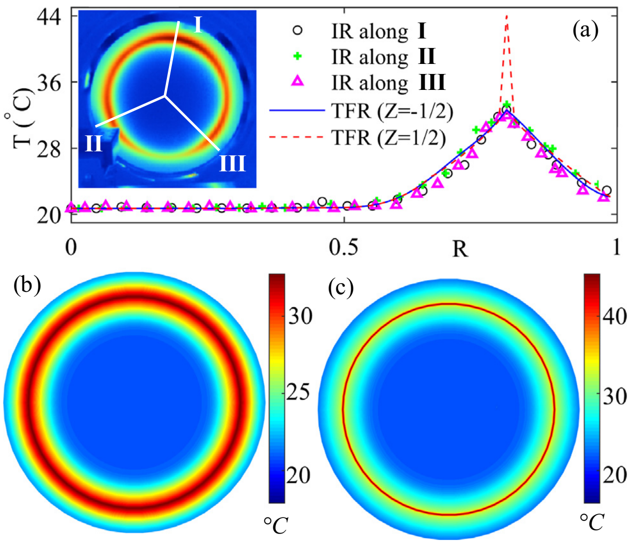

Fig. 10. Reconstruction of steady-state temperature fields: (a) Experimental measurement and reconstruction along radii; (b) Reconstructed temperature on the measured surface; (c) Reconstructed temperature on the machined surface.

reconstructed temperature fields on the measured and machined surfaces are presented in Fig. 10(b) and (c).

6. Conclusions

A temperature field reconstruction (TFR) method is proposed as a simple and effective way to investigate the thermal dynamics of a thin-wall disk-like workpiece (WP) during a turning process. The WP thermal dynamics is formulated as a boundary value problem of a circular plate with axisymmetric heating, where the plate surfaces are subjected to convection and the perimetric boundary is insulated. Employing the modal expansion approach, the temperature field is decoupled into products of the temperature mode shapes and time-varying coefficients, where the coefficients are determined from a finite number of nodal measurements without knowledge of the heat source intensity. Numerical analysis has been carried out to demonstrate the proposed TFR method in terms of normalized eigenvalues, mode shapes and modal coefficients, and provides a guideline in determining the employed modes in reconstruction. The TFR method is verified with the simulated measurements using FEA, and the maximum percentage errors are 1.12% and 6.48% for the aluminum and titanium cases with computation time of 0.07 and 0.1 s, respectively. An illustrative application to process state monitoring is presented to investigate the transient and steady-state temperature fields during a turning process, where temperature distributions on both the measured and machined surfaces are reconstructed to justify the ability for real-time computing and online sensing in manufacturing.

Conflict of interest

The authors declared that there is no conflict of interest.

Acknowledgment

This work was supported by the National Basic Research Program of China (973 Program, Grant No. 2013CB035803), National Natural Science Foundation of China under Grant 51505164, and the U.S. National Science Foundation (Grant CMMI-1662700).

Appendix A

The closed-form solution to (2) is derived in the Green's function approach, where a general initial condition $\psi_0(r,z)$ is applied to (5):

$$\sum_{i=1}^{\infty}\sum_{j=0}^{\infty} q_{ij}(0)\Phi_{ij}(r,\theta)=\psi_0(r,z) \tag{A1}$$

Multiplying both sides of (A1) by $r\Phi_{i'j'}(r,\theta)$ and integrating over the plate cross-section

$$\sum_{i=1}^{\infty}\sum_{j=0}^{\infty}\int_{-h/2}^{h/2}\int_{0}^{a} q_{ij}(0)\Phi_{ij}(r',z')\Phi_{i'j'}(r',z')r'dr'dz' = \int_{-h/2}^{h/2}\int_{0}^{a}\psi_0(r',z')\Phi_{i'j'}(r',z')r'dr'dz',$$

produces the expression for $q_{ij}(0)$

$$q_{ij}(0)=\frac{1}{\eta_{ij}}\int_{-h/2}^{h/2}\int_{0}^{a}\psi_0(r',z')\Phi_{ij}(r',z')r'dr'dz'. \tag{A2}$$

where the orthogonality among mode shapes is employed

$$\int_{-h/2}^{h/2}\int_{0}^{a}\Phi_{ij}(r',z')\Phi_{i'j'}(r',z')r'dr'dz' = \begin{cases} 0 & \text{if } i'=i, j'=j \\ \eta_{ij} & \quad i'\neq i, j'\neq j \end{cases}. \tag{A3}$$

With $\Phi_{ij}(r,z)=J_0(\delta_i r)\cos\left[\beta_j z-\frac{1-(-1)^j}{4}\pi\right]$, η_{ij} can be obtained as

$$\eta_{i0}=\frac{\beta_0 h+S_{\beta_0 h}}{2\beta_0}\frac{a^2J_0^2(\delta_i a)}{2},\quad \eta_{ij}=\frac{a^2hJ_0^2(\delta_i a)}{4}\quad (j=1,2,\ldots). \tag{A4}$$

The response to the initial condition $\psi_0(r,z)$ is

$$\psi_{in}(t,r,z)=\sum_{i=1}^{\infty}\sum_{j=0}^{\infty}\frac{e^{-\alpha\lambda_{ij}^2 t}\Phi_{ij}(r,z)}{\eta_{ij}}\int_{-h/2}^{h/2}\int_0^a \Phi_{ij}(r',z')\psi_0(r',z')r'dr'dz';$$

at the same time, $\psi_{\text{in}}(r, z)$ can also be given from the Green's function approach [47]:

$$\psi_{in}(t,r,z)=\int_{-h/2}^{h/2}\int_0^a G(t,r,z;t',r',z')|_{t'=0}\psi_0(r',z')r'dr'dz'$$

As the above two equations are valid for any $\psi_0(r, z)$, the Green's function can be obtained as

$$G(t,r,z;t',r',z')=\sum_{i=1}^{\infty}\sum_{j=0}^{\infty}\frac{1}{\eta_{ij}}e^{-\alpha\lambda_{ij}^2(t-t')}\Phi_{ij}(r,z)\Phi_{ij}(r',z') \tag{A5}$$

Then the closed-form solution to the BVP (2) and (2′) is

$$\psi(t,r,z)=\int_{-h/2}^{h/2}\int_0^a G(t,r,z;t',r',z')|_{t'=0}(T_0-T_\infty)r'dr'dz'+\cdots$$
$$\frac{\alpha}{k_t}\int_0^t\int_{-h/2}^{h/2}\int_0^a G(t,r,z;t',r',z')g(t',r',z')r'dr'dz'dt'$$

For a special case when $T_0 = T_\infty$ and $g(t;\, r,\, z;\, r_c,\, z_c)=1(t)\delta(r-r_c)\delta(z-z_c)$,

$$\psi(t,r,z)=\sum_{i=1}^{\infty}\sum_{j=0}^{\infty}\frac{1-e^{-\alpha\lambda_{ij}^2 t}}{k_t\eta_{ij}\lambda_{ij}^2}r_c\Phi_{ij}(r_c,z_c)\Phi_{ij}(r,z) \tag{A6}$$

In summary, the solution to the BVP (1) and (1′) given by $T = T_0 + \psi$ can be rewritten as

$$T(t,r,z)=T_0+\sum_{i=1}^{\infty}\sum_{j=0}^{\infty}q_{ij}(t)\Phi_{ij}(r,z) \tag{A7}$$

where the modal coefficients in (A7) and (5) are given as

$$q_{i0}(t)=\frac{\beta_0}{\beta_0 h+S_{\beta_0 h}}\frac{4r_c\Phi_{ij}(r_c,z_c)}{k_t a^2 J_0^2(\delta_i a)}\frac{1-e^{-\alpha\lambda_{ij}^2 t}}{\lambda_{ij}^2},$$
$$q_{ij}(t)=\frac{4r_c\Phi_{ij}(r_c,z_c)}{k_t h a^2 J_0^2(\delta_i a)}\frac{1-e^{-\alpha\lambda_{ij}^2 t}}{\lambda_{ij}^2}\quad(j=1,2,\ldots). \tag{A8}$$

Appendix B

It can be obtained from (8f) that

$$\frac{\gamma_{00}}{\gamma_{10}}=\frac{\lambda_{10}^2\int_0^a\int_{-h/2}^{h/2}r'\Phi_{10}^2(r',z')dr'dz'}{\lambda_{00}^2\int_0^a\int_{-h/2}^{h/2}r'\Phi_{00}^2(r',z')dr'dz'} \tag{B1}$$

where $\Phi_{i0}(r',z')=J_0(\delta_i r')\cos(\beta_0 z'),\lambda_{i0}^2=\delta_i^2+2k_c/(hk_t)$, $i = 0$ and 1. Given the identity

$$\int_0^a r'\Phi_{i0}^2(r',z')dr'=\frac{1}{2}a^2J_0^2(a\delta_i)$$

(B1) is rewritten as

$$\frac{\gamma_{00}}{\gamma_{10}}=\frac{J_0^2(a\delta_1)}{J_0^2(a\delta_0)}\left(1+\frac{\delta_1^2 k_t h a^2}{2k_c}\right) \tag{B2}$$

or in terms of normalized eigenvalues

$$\frac{\gamma_{00}}{\gamma_{10}}=\frac{J_0^2(\bar{\delta}_1)}{J_0^2(\bar{\delta}_0)}\left(1+\frac{\bar{\delta}_1^2}{2\pi k_c}Vk_t\right) \tag{B3}$$

where $V=\pi a^2 h$.

References

[1] W.B. Rashid, S. Goel, X. Luo, J.M. Ritchie, The development of a surface defect machining method for hard turning processes, Wear 302 (1) (2013) 1124–1135.

[2] E. Capello, Residual stresses in turning: Part II. Influence of the machined material, J. Mater. Process. Technol. 172 (3) (2006) 319–326.

[3] M.U. Ghani, N.A. Abukhshim, M.A. Sheikh, An investigation of heat partition and tool wear in hard turning of H13 tool steel with CBN cutting tools, Int. J. Adv. Manuf. Technol. 39 (9) (2008) 874–888.

[4] D. O'Sullivan, M. Cotterell, Temperature measurement in single point turning, J. Mater. Process. Technol. 118 (1) (2001) 301–308.

[5] S. Chinchanikar, S. Choudhury, A. Kulkarni, Investigation of chip-tool interface temperature during turning of hardened AISI 4340 alloy steel using multi-layer coated carbide inserts, in: Advanced Materials Research, Trans Tech Publ., 2013, pp. 354–358.

[6] A.E. Segall, Solutions for the correction of temperature measurements based on beaded thermocouples, Int. J. Heat Mass Transf. 44 (15) (2001) 2801–2808.

[7] D. O'Sullivan, M. Cotterell, Workpiece temperature measurement in machining, Proc. Inst. Mech. Eng., Part B: J. Eng. Manuf. 216 (1) (2002) 135–139.

[8] L. Chen, B.L. Tai, R.G. Chaudhari, X. Song, A.J. Shih, Machined surface temperature in hard turning, Int. J. Mach. Tools Manuf 121 (2017) 10–21.

[9] H. Ay, W.-J. Yang, Heat transfer and life of metal cutting tools in turning, Int. J. Heat Mass Transf. 41 (3) (1998) 613–623.

[10] J.C. Heigel, E. Whitenton, B. Lane, M.A. Donmez, V. Madhavan, W. Moscoso-Kingsley, Infrared measurement of the temperature at the tool–chip interface while machining Ti–6Al–4V, J. Mater. Process. Technol. 243 (2017) 123–130.

[11] Z. Wei, K.-M. Lee, S.W. Tchikanda, Z. Zhou, S.-P. Hong, Effects of radiative transfer modeling on transient temperature distribution in semitransparent glass rod, J. Heat Transf. 125 (4) (2003) 635–643.

[12] M. Yu, J. Guo, K.-M. Lee, A modal expansion method for displacement and strain field reconstruction of a thin-wall component during machining, IEEE/ASME Trans. Mechatron. (2018).

[13] K.-M. Lee, L. Yang, K. Bai, J. Ji, An efficient flexible division algorithm for predicting temperature-fields of mechatronic system with manufacturing applications, IEEE/ASME Trans. Mechatron. 22 (4) (2017) 1818–1827.

[14] S. Rajashekhar Reddy, M.S. Kumar, V. Vasu, Temperature study in Turning Inconel-718: 3D simulation and experimentation, Mater. Today: Proc. 4 (9) (2017) 9946–9950.

[15] K.S. Sangwan, G. Kant, A. Deshpande, P. Sharma, Modeling of stresses and temperature in turning using finite element method, in: Applied Mechanics and Materials, Trans Tech Publ, 2013, pp. 174–177.

[16] F. Samadi, F. Kowsary, A. Sarchami, Estimation of heat flux imposed on the rake face of a cutting tool: a nonlinear, complex geometry inverse heat conduction case study, Int. Commun. Heat Mass Transfer 39 (2) (2012) 298–303.

[17] M.V. Ramesh, K.N. Seetharamu, N. Ganesan, G. Kuppuswamy, Finite element modelling of heat transfer analysis in machining of isotropic materials, Int. J. Heat Mass Transf. 42 (9) (1999) 1569–1583.

[18] A. Deshpande, V. Madhavan, A novel approach to accelerate attainment of thermal steady state in coupled thermomechanical analysis of machining, Int. J. Heat Mass Transf. 55 (13) (2012) 3869–3884.

[19] H. Yapıcı, M.S. Genç, G. Özışık, Transient temperature and thermal stress distributions in a hollow disk subjected to a moving uniform heat source, J. Therm. Stresses 31 (5) (2008) 476–493.

[20] K.S. Parihar, S.S. Patil, Transient heat conduction and analysis of thermal stresses in thin circular plate, J. Therm. Stresses 34 (4) (2011) 335–351.

[21] K.R. Gaikwad, X.-J. Yang, Two-dimensional steady-state temperature distribution of a thin circular plate due to uniform internal energy generation, Cogent Math. 3 (1) (2016) 1135720.

[22] M.N. Gaikwad, K.C. Deshmukh, Thermal deflection of an inverse thermoelastic problem in a thin isotropic circular plate, Appl. Math. Model. 29 (9) (2005) 797–804.

[23] K.R. Gaikwad, K.P. Ghadle, Nonhomogeneous heat conduction problem and its thermal deflection due to internal heat generation in a thin hollow circular disk, J. Therm. Stresses 35 (6) (2012) 485–498.

[24] A.K. Tikhe, K.C. Deshmukh, Inverse heat conduction problem in a thin circular plate and its thermal deflection, Appl. Math. Model. 30 (6) (2006) 554–560.

[25] M.M. Roozbahani, H. Razzaghi, M. Baghani, M. Baniassadi, M. Layeghi, Temperature and stress distribution in hollow annular disk of uniform thickness with quadratic temperature-dependent thermal conductivity, J. Therm. Stresses 40 (7) (2017) 828–845.

[26] K.C. Deshmukh, S.D. Warbhe, V.S. Kulkarni, Quasi-static thermal deflection of a thin clamped circular plate due to heat generation, J. Therm. Stresses 32 (9) (2009) 877–886.

[27] F. Wang, Q. Ma, W. Meng, Z. Han, Experimental study on the heat transfer behavior and contact pressure at the casting-mold interface in squeeze casting of aluminum alloy, Int. J. Heat Mass Transf. 112 (2017) 1032–1043.

[28] C.-Y. Yang, Inverse determination of heat input during the friction stir welding process, Int. J. Heat Mass Transf. 76 (2014) 411–418.

[29] D. Weisz-Patrault, A. Ehrlacher, N. Legrand, Evaluation of temperature field and heat flux by inverse analysis during steel strip rolling, Int. J. Heat Mass Transf. 55 (4) (2012) 629–641.

[30] R.F. Brito, S.R. Carvalho, S.M.M. Lima, E Silva, Experimental investigation of thermal aspects in a cutting tool using comsol and inverse problem, Appl. Therm. Eng. 86(Suppl. C) (2015) 60–68.

[31] A. Bilbao Guillerna, D. Axinte, J. Billingham, The linear inverse problem in energy beam processing with an application to abrasive waterjet machining, Int. J. Mach. Tools Manuf 99 (2015) 34–42.
[32] M. Hribersek, V. Sajn, F. Pusavec, J. Rech, J. Kopac, The procedure of solving the inverse problem for determining surface heat transfer coefficient between liquefied nitrogen and Inconel 718 workpiece in cryogenic machining, Proc. CIRP 58 (2017) 617–622.
[33] P. Kwon, T. Schiemann, R. Kountanya, An inverse estimation scheme to measure steady-state tool–chip interface temperatures using an infrared camera, Int. J. Mach. Tools Manuf 41 (7) (2001) 1015–1030.
[34] T. Abdelhamid, A.H. Elsheikh, A. Elazab, S.W. Sharshir, E.S. Selima, D. Jiang, Simultaneous reconstruction of the time-dependent Robin coefficient and heat flux in heat conduction problems, Inverse Prob. Sci. Eng. (2017) 1–18.
[35] S.R. Carvalho, S.M.M. Lima e Silva, A.R. Machado, G. Guimarães, Temperature determination at the chip–tool interface using an inverse thermal model considering the tool and tool holder, J. Mater. Process. Technol. 179 (1) (2006) 97–104.
[36] M. Mierzwiczak, J.A. Kołodziej, The determination temperature-dependent thermal conductivity as inverse steady heat conduction problem, Int. J. Heat Mass Transf. 54 (4) (2011) 790–796.
[37] V.M. Luchesi, R.T. Coelho, An inverse method to estimate the moving heat source in machining process, Appl. Therm. Eng. 45–46 (2012) 64–78.
[38] L. Cheng, F. Zhong, H. Gu, X. Zhang, Application of conjugate gradient method for estimation of the wall heat flux of a supersonic combustor, Int. J. Heat Mass Transf. 96 (2016) 249–255.
[39] I. Sirajul, S. Ismail, Meshless collocation procedures for time-dependent inverse heat problems, Int. J. Heat Mass Transf. 113 (2017) 1152–1167.
[40] Y. Gu, L. Wang, W. Chen, C. Zhang, X. He, Application of the meshless generalized finite difference method to inverse heat source problems, Int. J. Heat Mass Transf. 108 (2017) 721–729.
[41] V. Norouzifard, M. Hamedi, A three-dimensional heat conduction inverse procedure to investigate tool–chip thermal interaction in machining process, Int. J. Adv. Manuf. Technol. 74 (9) (2014) 1637–1648.
[42] V. Norouzifard, M. Hamedi, Experimental determination of the tool–chip thermal contact conductance in machining process, Int. J. Mach. Tools Manuf. 84(Suppl. C) (2014) 45–57.
[43] N.A. Abukhshim, P.T. Mativenga, M.A. Sheikh, Heat generation and temperature prediction in metal cutting: a review and implications for high speed machining, Int. J. Mach. Tools Manuf. 46 (7–8) (2006) 782–800.
[44] C. Wagner, Heat transfer from a rotating disk to ambient air, J. Appl. Phys. 19 (9) (1948) 837–839.
[45] L.M. Yang, K.-M. Lee, K. Bai, Thermal field modeling algorithm based on flexible space division for high-power, high-precision mechatronic systems, in: 2014 IEEE/ASME International Conference on Advanced Intelligent Mechatronics, 2014, pp. 742–747.
[46] J. Ji, Y. Huang, K.-M. Lee, Cutting tool temperature field reconstruction using hybrid macro/micro scale modeling for machining of titanium alloy, in: 2016 IEEE International Conference on Advanced Intelligent Mechatronics (AIM), 2016, pp. 1265–1270.
[47] D.W. Hahn, M.N. Özişik, Heat Conduction, third ed., John Wiley & Sons, 2012.